QUARTERLY JOURNAL OF THE ROYAL METEOROLOGICAL SOCIETY
Q. J. R. Meteorol. Soc. **133**: 1677–1692 (2007)
Published online 27 September 2007 in Wiley InterScience
(www.interscience.wiley.com) DOI: 10.1002/qj.115

RMetS
ROYAL METEOROLOGICAL SOCIETY

Radar and *in situ* observations of small cumulus: physical interpretations of radar Bragg scatter

Brad Baker[a]* and Jean-Louis Brenguier[b]
[a] *SPEC Inc., Boulder, CO, USA*
[b] *Meteo-France (CNRM/GMEI), Toulouse, France*

ABSTRACT: Radar observations of small cumulus clouds are compared to predictions of radar measurements based on *in situ* measurements and the theory of radar back-scatter. At the wavelengths used, both Rayleigh and Bragg scatter can be important in small cumulus. A theoretical derivation of radar back-scatter from small cumulus clouds, in which both terms are succinctly derived using a common mathematical model, is presented.

For the earliest stages of cumulus clouds, the predictions of Bragg scatter, based on *in situ* measurements of water-vapour fluctuations, are in close agreement with radar-measured Bragg scatter. This suggests that the theory is adequate and our interpretations of the radar observations are correct. These interpretations include identifying regions where entrainment and mixing are ongoing, identifying adiabatic cores, and estimating the Kolmogorov microscale of turbulence.

As the small cumulus develop and enter the early collision and coalescence stages, another source of Bragg scatter can become significant. It is argued, via observations, that the additional Bragg scatter comes from anomalous liquid-water fluctuations. These liquid-water fluctuations are called 'anomalous' because they exceed what would result if liquid water mixed as a passive scalar. The Bragg scatter caused by liquid water may reach effective values of 5–10 dBZ, for a 3 cm-wavelength (X-band) radar, and thus confounds attempts to derive Rayleigh-scatter values below this level using a dual-wavelength (X- and S-band) radar system.

KEY WORDS adiabatic core; dual wavelength; entrainment; mixing

Received 7 April 2006; Revised 24 January 2007; Accepted 8 May 2007

1. Introduction

The purpose of this study is to identify the sources of Bragg scatter in small cumulus clouds and to provide physical interpretations of combined radar and airborne observations. Bragg scatter is a measure of the fluctuation of the atmosphere's electric permittivity on the spatial scale of half the radar wavelength. Data from the Small Cumulus Microphysics Studies (SCMS) project, which was designed to study the early development of precipitation in cumulus clouds, are analysed for this purpose. Knight and Miller (1998) summarize and discuss this project, and the dual-wavelength radar (CP-2/NCAR, S and X bands) used, including physical interpretations and how both Rayleigh and Bragg components may be derived from the two signals. The Rayleigh signal is used for the study of precipitation development. However, since the Bragg signal is also available, these data provide us with a good opportunity to study mixing in small cumulus. The use of radar, which can observe the entire cloud, to study mixing could have an advantage over the use of aircraft *in situ* observations, which are limited in coverage.

Before the Bragg signal may be confidently used to study mixing in clouds, it is first necessary to verify that the sources of Bragg scatter are well understood. In this study, *in situ* aircraft measurements (C-130/NCAR, Merlin/Meteo-France) are used to estimate the Bragg-scatter signals, and these are compared with the observed radar values. The radar equation, including both Rayleigh and Bragg terms, is derived in Appendix A using a single mathematical model. This allows us to refer explicitly to individual contributions to the Bragg scatter. These terms are then used in Appendix B, which shows how the radar Bragg scatter is estimated from *in situ* aircraft measurements.

Many of the radar observations and characteristics presented here are similar to those of Knight and Miller (1998). However, some of our interpretations differ from theirs. The main difference is in the determination of adiabatic cores in the early stage of the small cumulus, before collision and coalescence. During this early stage, Bragg scatter is dominated by water-vapour fluctuations, as expected (Gossard and Strauch, 1983). However, in more developed stages this is not always the case. Erkelens *et al.* (2001) review the data presented by Knight and Miller (1998), and present a number of theoretical arguments whereby the Bragg scatter in the interior of the cloud could be dominated by return from the droplets rather than water vapour. We will present

* Correspondence to: Brad Baker, SPEC Inc., 3022 Sterling Circle, Suite 200, Boulder, CO 80301, USA. E-mail: brad@specinc.com

evidence, based on comparisons between *in situ* aircraft and remote radar observations, demonstrating that the droplet contribution does indeed dominate under certain circumstances.

2. Terminology

When the scatterers are small in relation to the radar wavelength, the returned power can be closely approximated by the simple sum of two distinct terms, called the Rayleigh and Bragg terms. These two terms result from different physical aspects of the air being scanned (Gossard and Strauch, 1983). In Appendix A, both terms are derived using a single mathematical model of the physical situation. We include the derivation in this paper, firstly because other derivations use different mathematical models (one discrete and one continuous) for the two parts, and then add the terms together (Gossard and Strauch, 1983); and secondly because it allows us to refer to, and discuss, the various contributions to the radar measurement as explicit terms in an equation.

The Rayleigh term Z is strongly dependent on the size of the scatterers. For spherical particles it is proportional to the sixth moment of the particle-size distribution. Thus it can be used to observe the growth of the hydrometeors.

The other term is often called Bragg scatter, and this is the central subject of this study. It is caused by spatial fluctuations in the electric permittivity, dielectric constant, or electric susceptibility of the medium. Since entrainment and mixing generate such fluctuations, Bragg scatter can be used to explore these processes. During the early stages of cumulus-cloud formation, the droplets are small (with radii of the order of 10 μm), and for radar wavelengths greater than a few centimetres the Bragg term dominates the signal. As the droplets grow larger, first by condensation and then by collision and coalescence, the magnitude of the Rayleigh term increases, until it equals, and then exceeds and dominates, the Bragg term. Thus, although the radar may display dBZ, when observing small cumulus it should be remembered that this is an *effective* dBZ, since the signal can be influenced, if not dominated, by Bragg scatter. The effective dBZ for the X- and S-band radar will be denoted by dBZ_{eX} and dBZ_{eS} respectively. The actual reflectivity, once the Bragg component of the effective reflectivity has been removed, will be denoted by dBZ. The Bragg component of the effective reflectivity will be denoted by dBB: this is what an S-band (10 cm) radar would display as its effective reflectivity (dBZ_{eS}) if its signal consisted of the Bragg term alone. The method of deriving dBZ and dBB estimates from measurements of dBZ_{eX} and dBZ_{eS} is described in (Knight and Miller, 1998).

The value of dBB can also be predicted from *in situ* aircraft measurements. In Appendix B, the radar equation derived in Appendix A is rewritten in terms of quantities measured *in situ* with airborne instruments, and the method of estimating radar returns from *in situ* data is shown. This derivation separates, as individual terms, the various sources of Bragg scatter, including fluctuations in water vapour and liquid water.

3. Direct comparison for small clouds

In the early stage of small cumulus, before collision and coalescence, there is very good agreement between radar measurements and the predictions of theory and aircraft measurements. At this stage, both radar signals are typically dominated by Bragg scatter. The following example comes from the Meteo-France Merlin-IV aircraft, flown at an altitude of about 1.2 km along a near-radial towards the radar through small cumulus, which were forming in a line along a sea-breeze front. Figure 1(a) shows the radar data for two cumuli that the aircraft penetrated. The lower panel shows the measured dBZ_{eX}, while the middle panel shows the values of dBB inferred from dBZ_{eX} and dBZ_{eS}, with the approximate aircraft track superimposed (dashed red line). The upper panel shows the series of dBB values derived from the theory using the data measured *in situ* with the aircraft along this track. These data are shown in the upper three panels of Figure 1(b) (water vapour, liquid water, and temperature). The bottom panel in Figure 1(b) shows the contributions to the relative electric permittivity (Equation (15)) from water vapour, liquid water content and temperature, using the same colour codes as in the panels above.

Both the radar and the aircraft measurements shown in Figure 1 are typical of the clouds of that size on that morning. The Bragg echoes were especially strong on that day because of the relative dryness of the air entrained into the clouds. The predicted values are in the range 8 to 14 dBB at the cloud edges, and −15 to 2 dBB in the cloud cores; these are consistent with the radar measurements. The lowest dBB estimates are not found in these radar pictures, because of the larger sample volume of the radar measurements. At this stage, there is no retrievable dBZ signal because both radar signals are dominated by Bragg scatter.

The Bragg echo is due to fluctuations, caused by mixing, which are most intense at a thermal's edges, where the moister thermal air meets the drier air surrounding the thermal. This results in the inverted-bowl shape of the high-Bragg-echo region, often called a 'mantel echo'. Dry thermals exhibit the same pattern (Gossard and Strauch, 1983).

The bottom panel in Figure 1(b) demonstrates that the water-vapour contribution is dominant, confirming the estimates of Gossard and Strauch (1983). Since droplets keep cloudy air at or near saturation, water-vapour fluctuations must be well correlated with temperature fluctuations. In clear air, and to some extent at cloud edges, water-vapour fluctuations are probably due to incomplete mixing of air masses with different vapour contents.

On days moister than 6 August 1995, the Bragg scatter was correspondingly less intense. Its magnitude is still well predicted by the aircraft measurements, in the small-cumulus stage before collision and coalescence. Figure 2(a) shows radar-observed values of dBB and

DOI: 10.1002/qj

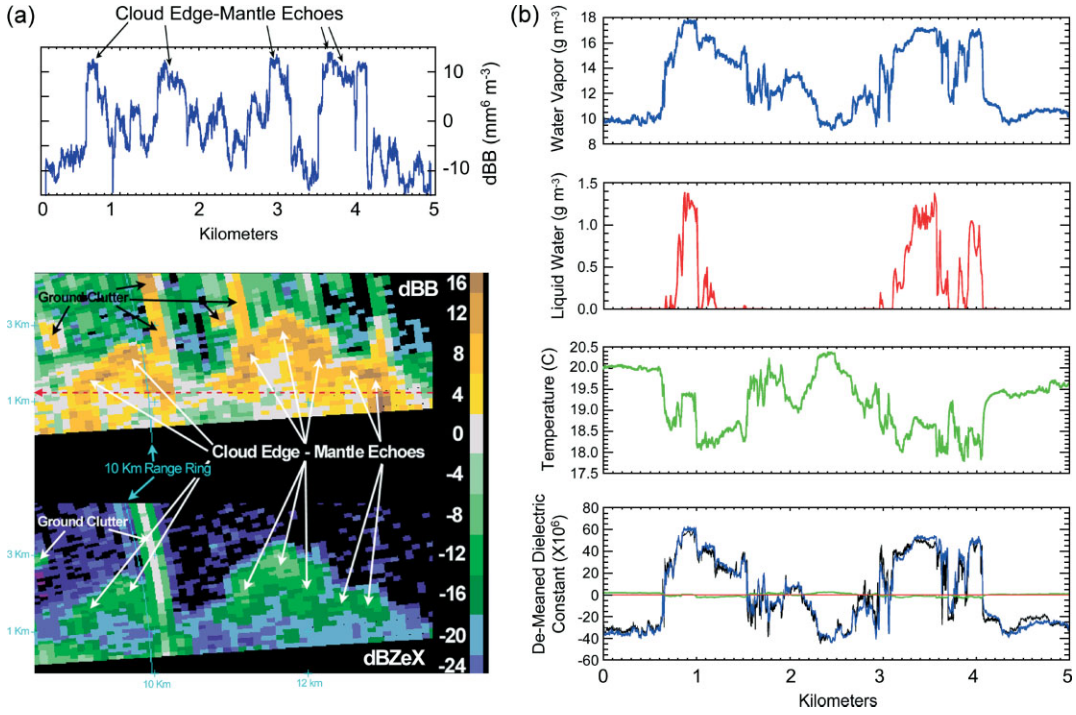

Figure 1. (a) Upper panel: time series of dBB values predicted from aircraft measurements through two small cumuli on 6 August 1995. Middle panel: radar display of dBB for the same clouds penetrated by the Merlin aircraft. Lower panel: radar display of dBZ_{eX}. The dashed red line indicates the approximate path of the aircraft. The time series and radar images are scaled, each showing about 5 km, to facilitate comparison. The zero distance of the time-series scale corresponds approximately to the right-hand edge of the radar display (about 13.5 km range). Exact correspondence between the panels is not to be expected, as the aircraft was slightly displaced from the radar measurement in both space and time. (b) *In situ* measurements from the aircraft. The top three panels show water-vapour content, liquid-water content, and temperature. The bottom panel shows the contributions of each of these variables to the relative electric permittivity (dielectric constant) according to Equation (15). Also shown, in black, is the relative electric permittivity measured independently with a refractometer. Since it is the fluctuation rather than the absolute value that is important, the mean value has been subtracted.

dBZ, together with aircraft-predicted dBB values, for an interesting pair of clouds on 22 July 1995. A detectable but weak dBZ signal exists for these taller clouds. The mantel echoes are similar, differing only in magnitude from those of 6 August (Figure 1(a)). The predicted Bragg scatter for the cloud edges on 22 July is about 0 to 12 dBB (Figure 2(a)), which is similar to the radar-observed values. The predicted value for the interior of the cloud thermals is around -8 to -1 dBB, which is also consistent with the radar-observed values. Figure 2(b) shows a cloud before collision and coalescence, from a day with an even moister environment, and so even weaker Bragg scatter, than that shown in Figures 1(a) and 2(a). The radar signal, about 2 to 7 dBB at the edges, is again well predicted by the aircraft measurements.

Incidentally, the cloud on the right-hand side of Figure 2(a) appears to be composed of two superimposed but separate thermal elements. The importance of the multi-thermal nature of cumulus clouds has been explored by Mason and Jonas (1974) and Blyth and Latham (1997).

4. Adiabatic cores

Like radar observations, aircraft measurements typically show more mixing near the cloud edge than in the centre. Occasionally an interior region has fluctuations so low that the region is thought to be adiabatic (Jensen *et al.*, 1985; Lawson and Blyth, 1998). Similarly and analogously, the Bragg-signal intensity of a cloud's interior region is occasionally found to be especially low: for example, see Figure 3. In Figure 3, the aircraft penetration was through a cloud similar and near to that shown on the radar display. The prediction for dBB in what appears to be an adiabatic region is about -10 dB. The especially-low dBB values measured by the radar are also about -10 dB. Therefore, we interpret such regions as adiabatic cores.

To be identifiable by radar, an adiabatic region must be at least as large as the radar pulse volume. The length of the radar samples, in the radial (range) direction, is 100 m. The samples are only semi-independent, as the radar pulse length is 150 m with samples taken at 100 m resolution. The width of the sample volume, in directions perpendicular to the radial direction, varies in direct proportion to the range, and is about 100 m at a range of about 15 km. The observations presented here were made at ranges of 4–21 km, with most between 10 km and 16 km. The aircraft probes have sample areas typically from a few square millimetres to a few square centimetres. In the direction of motion, their spatial resolution is typically 4–100 m, depending on the time response of the particular probe. Calculations for estimating dBB have been adjusted to yield independent

DOI: 10.1002/qj

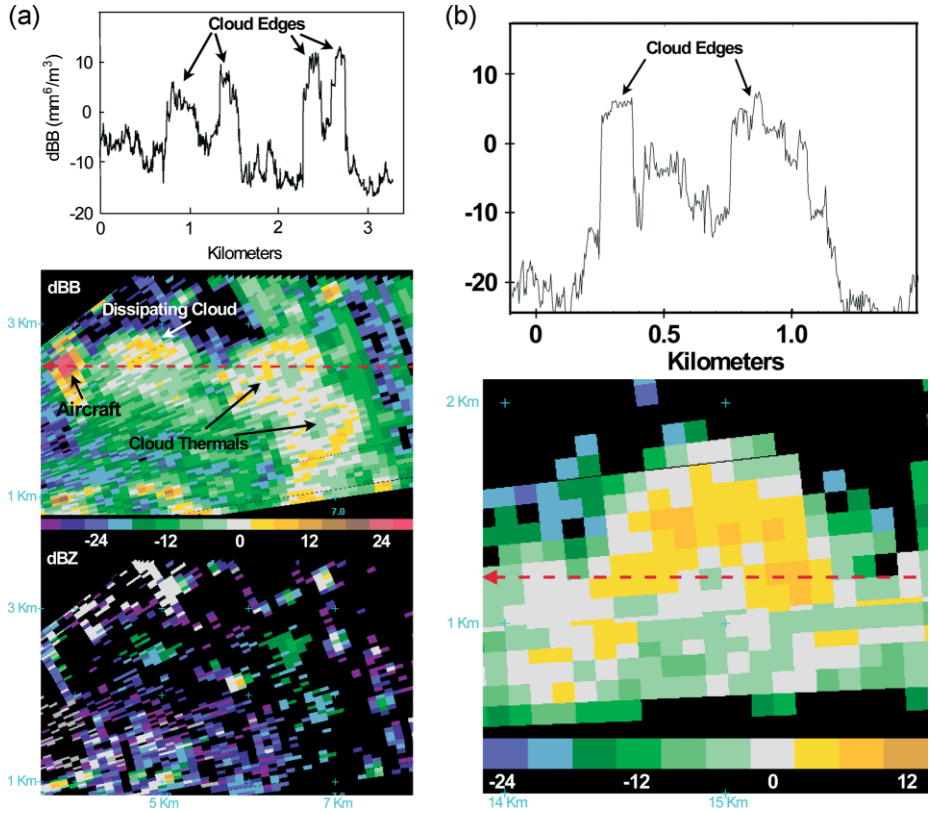

Figure 2. (a) Upper panel: aircraft-predicted values of dBB for a penetration of two clouds on 22 July 1995. Lower panels: radar displays of dBB and dBZ for the same clouds. Note that the radar detects the aircraft. (b) Radar display of dBB, and the predictions based on *in situ* measurements, made at an altitude of about 1.2 km, through the same cloud on 10 August 1995. As in Figure 1(a), dashed red lines indicate the approximate paths of the aircraft. The time series and radar images are scaled to facilitate comparison, and the zero distances of the time-series scales correspond approximately to the right-hand edges of the radar displays.

samples at about 100 m resolution. Thus, in the direction of motion, the aircraft estimates approximately match the radar's resolution. However, in the other directions, the aircraft sample lengths are many orders of magnitude smaller. The large radar sample volume, as compared with the aircraft sample volume, explains why adiabatic values are more common in the aircraft estimates – that is, why the lowest predicted dBB values in Figures 1 and 2 do not appear in the corresponding radar images.

While the mantel echo is typical for small cumulus clouds, only rare cases have sufficiently low Bragg intensity in the interior to suggest adiabaticity by our interpretation. This is consistent with what we would expect from SCMS aircraft observations of adiabatic cores. Lawson and Blyth (1998) have searched every aircraft penetration of five SCMS research days, and rarely found adiabatic regions larger than 100 m in length. Blyth *et al*. (2005) have looked at the percentage of 10 Hz aircraft samples (about 10 m spatially-averaged data) that had liquid-water content greater than 80% of the estimated adiabatic value. Just above cloud base, it was only 18%. At 300 m and 1 km above cloud base, it was just under 8%; and at 2 km above cloud base, it was less than 4%. Given the much-larger sample volume of the radar, we would expect radar observations of adiabatic cores to be considerably less common (Here we mean less common in terms of the percentage of observations that indicate adiabatic ascent. Since the radar in SCMS sampled many more clouds than the aircraft did, the total number of adiabatic radar observations could be greater than the total number from aircraft.) than aircraft observations of adiabatic samples; indeed, cases like that shown in Figure 3 are very rare.

Knight and Miller (1998) interpret *relatively-horizontal* X-band radar contours as indicative of adiabatic cores. Although they do not quantify how horizontal the contours should be to indicate adiabatic cloud, they do show six examples that they believe are sufficiently horizontal to indicate adiabatic ascent. Their interpretation and examples suggest a more frequent occurrence of adiabatic cores than is indicated by our interpretation.

In an adiabatic parcel, droplets grow with ascent and shrink with descent. Therefore, horizontal variations in reflectivity are small compared with vertical variations in reflectivity, and this creates relatively-horizontal contours. However, it is also true that in non-adiabatic parcels, droplets tend to grow with ascent and shrink with descent. Only with quite a large horizontal variation in droplet concentration or liquid-water content would the X-band contours not be relatively-horizontal. Adiabaticity is destroyed by entrainment. Entrainment is, essentially, cloud mixing with environment. Mixing continues and reduces the gradients created by entrainment. Thus, it is feasible to have had entrainment (non-adiabatic

DOI: 10.1002/qj

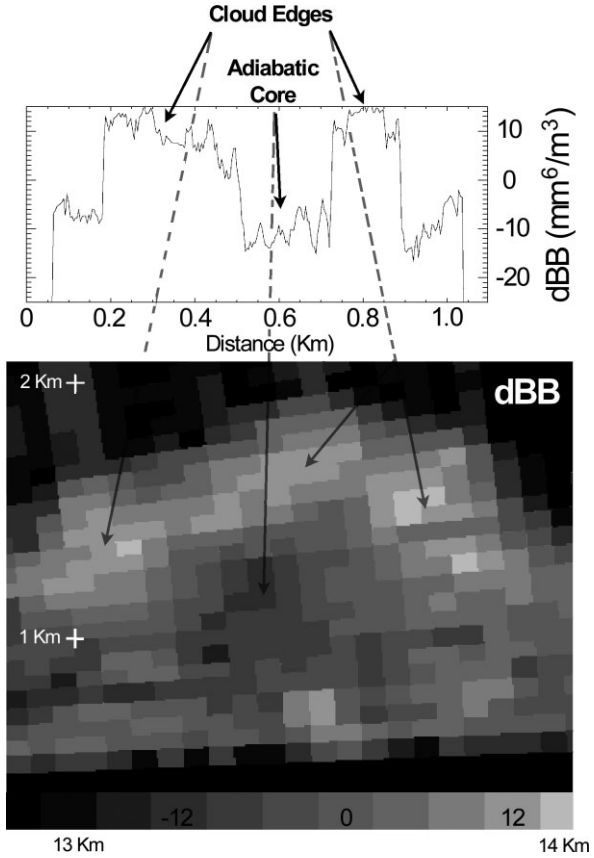

Figure 3. Lower panel: radar-measured dBB for a small cumulus on 6 August 1995 that has unusually low values in the interior, interpreted here as an adiabatic core. Upper panel: predictions from *in situ* measurements made at an altitude of about 1.3 km in a similar nearby small cumulus with a large adiabatic core.

cloud) and horizontal gradients small enough to cause relatively-horizontal radar contours. The same applies to our method of identification of adiabatic cores. Theoretically, post-entrainment mixing could reduce the gradients to yield very low dBB values. The relevant length scales of the gradients differ between cases, as do the sensitivities of the methods to those gradients. We argue that low dBB values constitute a more sensitive signature of adiabatic cloud regions than relatively-horizontal contours, and that relatively-horizontal contours may be interpreted as indicative of sustained updraught.

Knight and Miller (1998, figures 8 and 9) show a consistency between the assumption of adiabatic ascent, a simple drop-growth model, and the measured dBZ values. However, their analysis does not demonstrate sensitivity to breaching the assumption of adiabatic ascent; therefore, it does not convincingly prove that the case shown is one of adiabatic ascent. Nevertheless, we agree with Knight and Miller's point that such analysis could be useful for estimating cloud properties from radar measurements.

5. Cloud sizes

Depending on range and sensitivity, the Rayleigh echo from small droplets may be too weak to be detected. Hence, Rayleigh echoes do not always reveal the entire cloud. The Bragg echo, on the other hand, typically reveals the edges of thermals, wet or dry. Thus, the Bragg echo can be a better measure of a cloud's true extent. However, one cannot equate the Bragg mantel echo with the liquid-water cloud, because a cloud can partially or totally evaporate, and the remaining water-vapour fluctuations can create a Bragg echo that looks the same as if a liquid-water cloud were still there. An example is shown in Figure 1(a). The aircraft flew from right to left in the radar picture, and thus, according to the radar, it penetrated a larger cloud first and then a smaller one. But the aircraft liquid-water trace indicates just the opposite. The small liquid-water cloud penetrated first is surrounded by a region of high humidity, with large fluctuations in the humidity. Note that the aircraft prediction of dBB does agree with the radar picture's cloud sizes. In this case, the thermal-like flow is large, and revealed by the Bragg echo, but the liquid-water cloud is much smaller. This was a rare case in the data we surveyed. It seems that these clouds do not usually detrain large amounts until they reach their maximum height, where they mix out and evaporate entirely. The example in Figure 1(a) is just at that stage. Once the liquid water had completely evaporated, the humidity fluctuations, and thus the Bragg echo, quickly weakened.

6. The Kolmogorov microscale

To predict dBB from aircraft measurements, and to derive dBB and dBZ from dBZ_{eS} and dBZ_{eX}, we assume that the humidity fluctuations obey Kolmogorov's scaling law for passive scalars in the inertial subrange of isotropic homogeneous turbulence. In the latter case, the assumption is that it holds for the specific range of scales between the two radar half-wavelengths, which is approximately 1.5–5 cm. In this case, when Bragg scatter dominates both radar signals, the difference between dBZ_{eS} and dBZ_{eX} should be about 19 dB (Knight and Miller, 1998). When the Rayleigh scatter begins to significantly affect the X-band signal, then $dBZ_{\mathrm{eS}} - dBZ_{\mathrm{eX}}$ falls below 19 dB, and when the Rayleigh scatter dominates both radar signals, $dBZ_{\mathrm{eS}} - dBZ_{\mathrm{eX}}$ should be zero.

Observations of $dBZ_{\mathrm{eS}} - dBZ_{\mathrm{eX}}$ often exceed 19 dB, however. Knight and Miller (1998) point out several explanations for this: the two radar volumes do not coincide exactly, which can cause $dBZ_{\mathrm{eS}} - dBZ_{\mathrm{eX}}$ to be artificially low or high where there are strong gradients in dBZ_{eX} or dBZ_{eS}; and there are statistical fluctuations, of a few decibels, due to averaging over a finite number of independent radar returns. We will now present and motivate another possible explanation.

Our hypothesis is that the Kolmogorov microscale is larger than 1.5 cm, so that the scaling laws of the inertial subrange do not apply in the range 1.5–5 cm, as assumed; rather, the energy spectrum falls off more steeply because of viscous effects.

This hypothesis is supported by previous work, in which the empirical microscale η_{t}, defined as the length

DOI: 10.1002/qj

scale at which viscous dissipation becomes significant, is found to be considerably larger than the scaling estimates η_e of it. Using measurements of geophysical fluid flows, Chapman (1979, figure 13) found η_t to be approximately $10 \times \eta_e$, where η_e was estimated as $LR^{-3/4}$. Here L is the length scale of the flow – cloud in this case – and R is the Reynolds number. For cumulus, this typically yields something of the order of a millimetre. Similarly, using data from (Hill, 1978), Gossard *et al.* (1984) found η_t to be $25 \times \eta_e$, where

$$\eta_e = \left(\frac{\nu^3}{\varepsilon}\right)^{\frac{1}{4}},$$

ν being the kinematic viscosity and ε the rate of energy dissipation. In fact, it is fair to say that Gossard *et al.* (1984) predict the result we hypothesize here.

Further motivation comes from averaging over a number of neighbouring radar volumes, particularly where gradients are weak. The process of averaging reduces the magnitude of the statistical causes of variation in $dBZ_{eS} - dBZ_{eX}$. We find that $dBZ_{eS} - dBZ_{eX}$ still tends to be greater than 19 dB for many of these cases. Figure 4 shows an example. Here $dBZ_{eS} - dBZ_{eX}$, averaged over the region inside the boundary shown, is greater than 22 dB.

The derivation of dBB and dBZ from dBZ_{eS} and dBZ_{eX} is largely unaffected by the breach of assumption implied by the above hypothesis. The predictions of dBB from the aircraft-measured water-vapour fluctuations are also largely unaffected. In this case, the assumption is that the scaling law holds from much larger scales of the *in situ* measurements, down to the 5 cm scale, which is still a good approximation for water vapour.

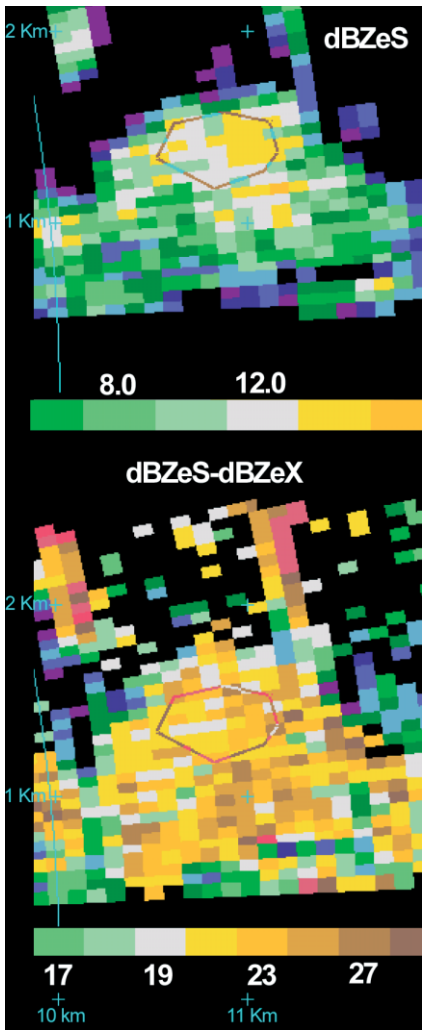

Figure 4. Plots of dBZ_{eS} and $dBZ_{eS} - dBZ_{eX}$ for a small cumulus dominated by Bragg scatter. The average value of $dBZ_{eS} - dBZ_{eX}$ in the outlined region is 22.4 dB.

7. An unexpected correlation for larger clouds

Predictions from *in situ* measurements agree well with radar observations of small cumulus whenever the cloud droplets are still primarily in the stage preceding collision and coalescence. As the clouds develop, the droplets grow larger and the Rayleigh term comes into play. Mixing in of dry air at the cloud edges reduces the number and size of the droplets. Thus, dBZ should be greatest in the cloud interior, and, since droplets grow as they ascend, dBZ should increase with height until the hydrometeors are large enough to descend by gravity. This evolution is typically observed in the derived dBZ data. It is also sometimes observed that dBB remains essentially unchanged as the droplet sizes increase: it remains greatest at the cloud edges, where mixing of cloudy and clear air first occurs. Figure 5 shows such a case, where the expected spatial anti-correlation between dBB and dBZ is apparent. This was typical when the Bragg scatter was very strong.

However, the opposite was observed when the magnitude of the Bragg scatter was much less (Figure 6(a)). The Bragg scatter is now greatest in the interior, and increases with height, much like the Rayleigh scatter. In this case dBB is spatially correlated with dBZ. Knight and Miller (1998) present this unexpected correlation in another way. They show that $dBZ_{eS} - dBZ_{eX}$ tends to a value of about 10 dB in these so-called 'mystery' echo clouds. Erkelens *et al.* (2001) review the data presented by Knight and Miller, and present a number of arguments whereby the Bragg scatter in the interior of the cloud could be dominated by return from the droplets rather than by water vapour. Below we present evidence for this explanation, based on the *in situ* and radar observations of SCMS. Coherent back-scattering from droplets may equivalently be called Bragg scatter from liquid-water fluctuations (Equation (17)). Erkelens *et al.*consider various explanations for how the liquid-water fluctuations could dominate the water-vapour fluctuations, including scenarios where liquid water mixes passively and scenarios where droplet inertia causes anomalous diffusion (clumping) of the droplets on centimetre scales. Figure 1(b) shows that the former scenario is not occurring in the SCMS cumulus, confirming the original comparison of the magnitude of the terms by Gossard and

DOI: 10.1002/qj

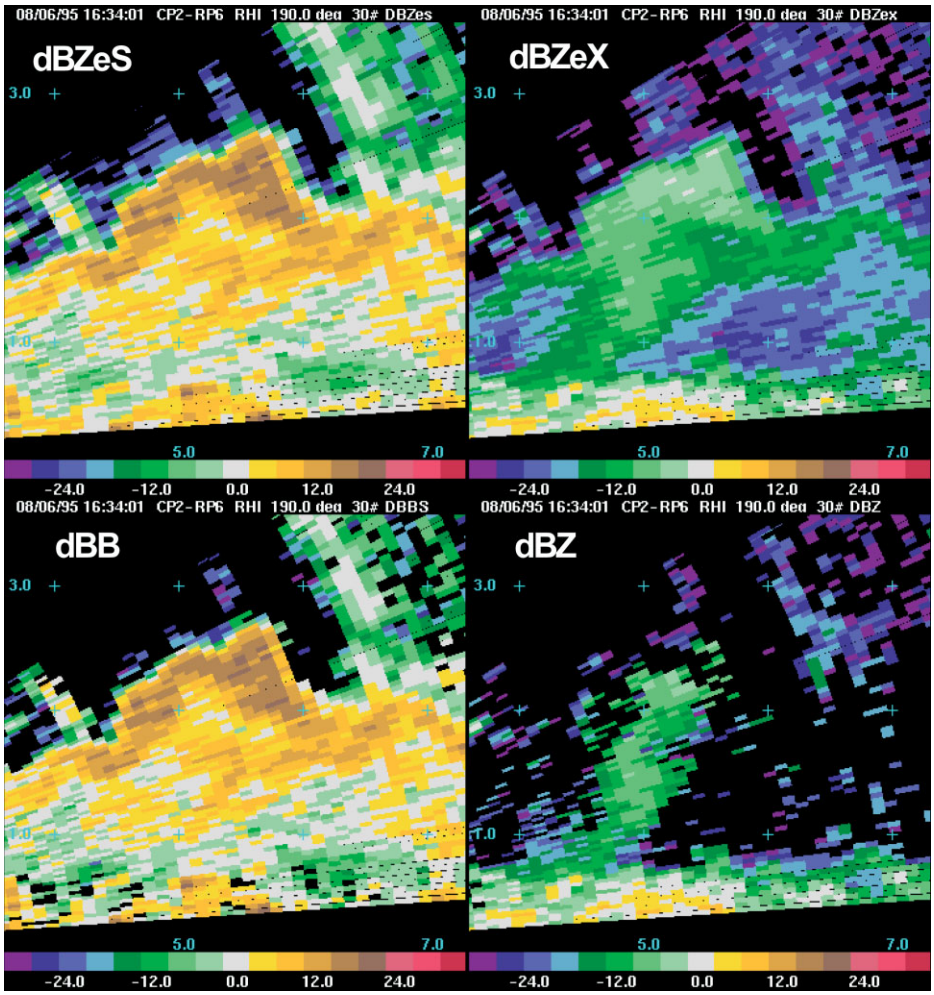

Figure 5. Plots of dBZ_{eS}, dBZ_{eX}, dBB and dBZ, for a cloud in the more-developed collision–coalescence stage, on 6 August 1995. The dBZ plot shows a light precipitation shaft, while the dBB plot shows strong mixing on the edges. Essentially dBZ_{eS} is equal to dBB, since even at this stage the S-band signal is still dominated by Bragg scatter, on this day. Note that dBZ_{eX} would be difficult to interpret alone. Its signal is dominated by Rayleigh scatter in some areas and by Bragg scatter in others.

Strauch (1983). By our interpretation of the data, the latter scenario is probably occurring. We call these liquid-water fluctuations 'anomalous' because they exceed those that would result if liquid water mixed as a passive scalar. In Figure 6(a), the Bragg scatter caused by liquid water reaches an effective value of about 4 dBZ for the 3 cm-wavelength (X-band) radar. It reaches higher values – but not more than 10 dBZ – in the general dataset. This confounds attempts to derive Rayleigh-scatter values below this level using a dual-wavelength (3 cm and 10 cm) radar system.

7.1. Observations and analysis

During SCMS there were far fewer penetrations at higher altitudes, where collision and coalescence were just beginning, than in the smaller early-stage cumulus. However, the Bragg scatter expected from water-vapour fluctuations at those higher altitudes can still be estimated from environmental soundings together with *in situ* measurements from lower altitudes. Assuming that, for a given field of clouds, the turbulent-mixing process is similar at all cloud heights h, the intensity of the Bragg scatter is simply proportional to the square of the difference in water-vapour content ρ_v between the cloudy and clear air being mixed (see Appendix B):

$$B(h) \propto \left(\Delta\rho_v(h)\right)^2.$$

The constant of proportionality is estimated from measurements in small cumulus, where it has already been demonstrated that Bragg scatter is due to water-vapour fluctuations. The quantity $(\Delta\rho_v(h))^2$ is estimated from the vertical soundings that were taken in the vicinity of the clouds by the aircraft. Two values of $(\Delta\rho_v(h))^2$ are estimated. One value is based on the difference between an adiabatic cloud parcel and the environment at the same height:

$$\Delta\rho_v(h) = \rho_{\text{adiabatic}}(h) - \rho_{\text{environment}}(h).$$

This represents the maximum possible $(\Delta\rho_v(h))^2$, and thus gives us a prediction for the magnitude of the Bragg scatter at the cloud edges. The second value provides an

DOI: 10.1002/qj

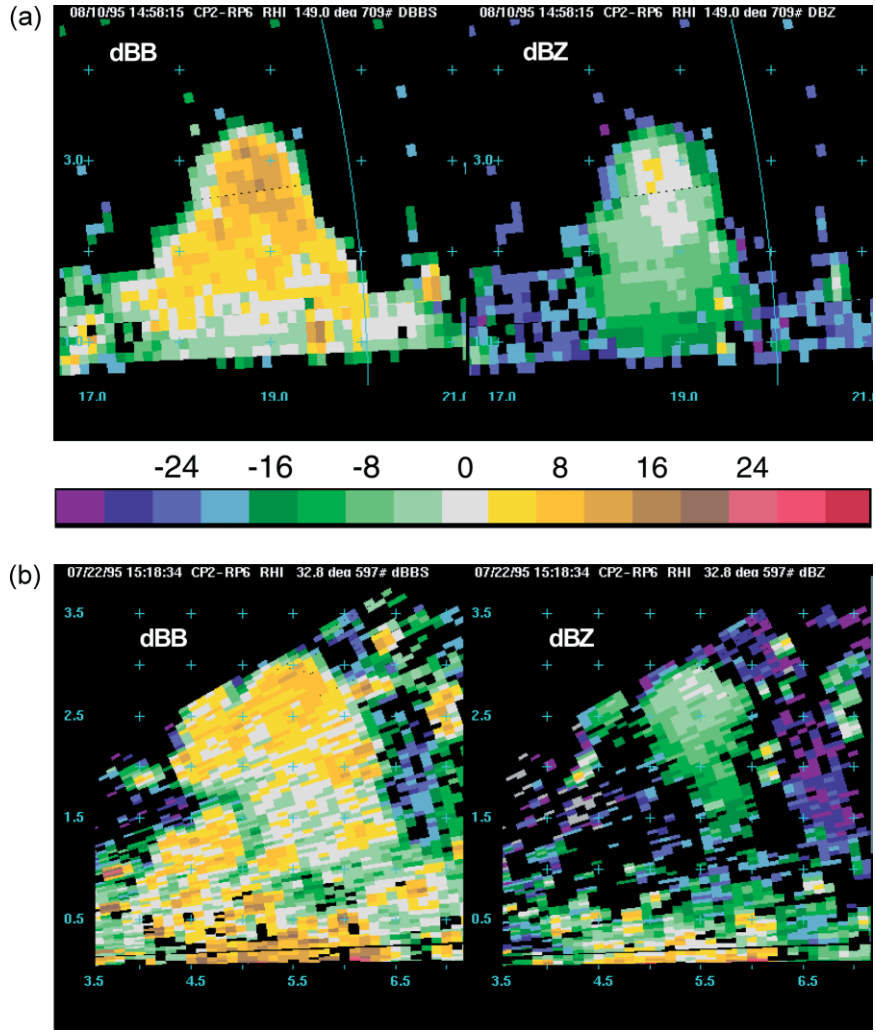

Figure 6. (a) The Bragg reflectivity pattern (dBB) and the Rayleigh reflectivity pattern (dBZ) for a cloud on 10 August 1995 that was beginning to produce precipitation-sized particles. At this stage of development it was common on this day for the Bragg reflectivity to be maximal high up and in the core of the cloud, much as the Rayleigh reflectivity is. Note the spatial correlation between the two signals in this picture, compared to the anti-correlation seen in Figure 5. (b) The Bragg and Rayleigh reflectivity patterns for a cloud on 22 July 1995 that was also beginning to produce precipitation-sized particles. On this day the maximum in the Bragg scatter is not clearly in the core, as in (a), nor is it clearly near the edge, as in Figure 5.

estimate for the cloud-interior maximum Bragg scatter by finding the maximum difference between an adiabatic parcel and all possible mixed parcels, assuming that the mixed parcels are saturated:

$$\Delta\rho_{\mathrm{v}}(h) = \max\left\{\rho_{\mathrm{adiabatic}}(h) - \rho_{\mathrm{mixed}}(h)\right\}.$$

Figure 7 shows the comparison for the cloud shown in Figure 5. This was a dry-environment day with large Bragg scatter, and the cloud had just begun to form precipitation. The agreement seen for the majority of the points suggests that the Bragg scatter at all levels in this cloud was caused by water-vapour fluctuations.

Figure 8 shows the comparison for the early-precipitating-stage cloud shown in Figure 6(a), on a moist-environment low-Bragg-scatter day. Contrary to predictions, an increase of Bragg scatter with altitude is observed, especially for the interior values, which reach 12 dBB in the upper portion of the cloud. Thus, the water-vapour fluctuations cannot account for the Bragg scatter, and there must be another source. Since Rayleigh scatter comes from cloud droplets, the spatial correlation between the Bragg and Rayleigh echoes (Figure 6(a)) suggests that the cloud droplets constitute this other source: in other words, the extra fluctuations in electric permittivity are due to fluctuations in the liquid-water content. This source of Bragg scatter is represented by Equation (17). Since the Bragg scatter is increasing with height, it seems that the liquid-water fluctuations are increasing as the liquid water itself increases, or, similarly, as the droplets grow larger.

Figure 9 shows a comparison like those of Figures 7 and 8, but from a day with intermediate moisture content. Figure 6(b) shows a radar image of this cloud. Here the cloud-edge values are reasonably consistent with the predictions, as in Figure 7, and so water-vapour fluctuations can account for the Bragg

DOI: 10.1002/qj

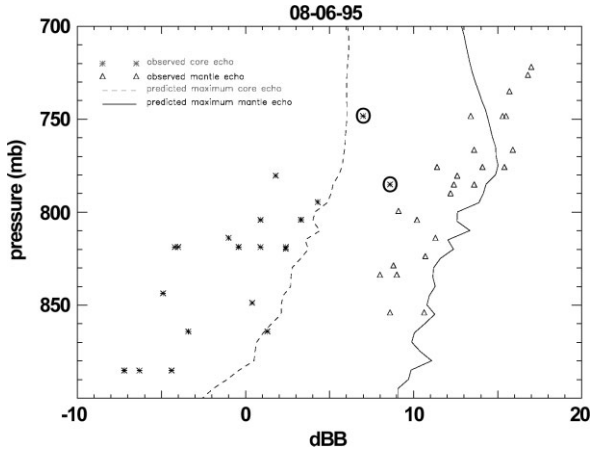

Figure 7. Predicted Bragg scatter, assuming that the water-vapour contribution is dominant, plotted against pressure (height), on 6 August 1995. The observed values are also plotted. The solid line and triangles represent the cloud edge; the dashed line and asterisks represent the cloud interior. The cloud-interior points that exceed the prediction are circled for emphasis. They are few, and do not greatly exceed the prediction.

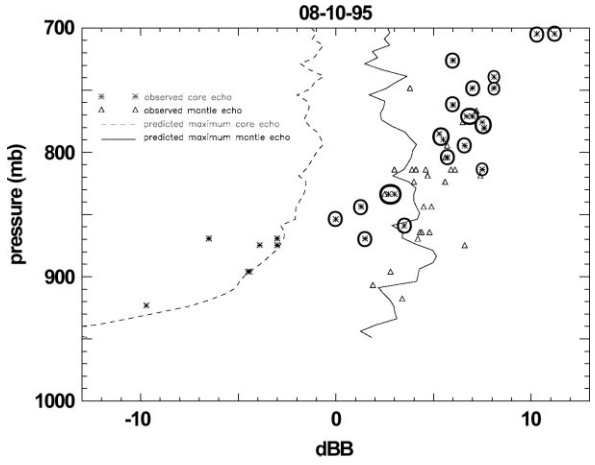

Figure 8. Predicted Bragg scatter, assuming that the water-vapour contribution is dominant, and the radar-observed values, plotted against pressure (height), on 10 August 1995. Lines and symbols are as in Figure 7. The cloud-interior points that exceed the prediction are circled for emphasis. There are many that greatly exceed the predictions.

scatter there. The cloud-interior observations, however, exceed the predictions, as in Figure 8, and so, by our interpretation, liquid-water fluctuations must account for the Bragg scatter there. In the upper cloud, values of 5–10 dBB are observed both in the interior and on the cloud edges, although the former are due to liquid-water fluctuations and the latter to water-vapour fluctuations. There is no clear maximum in the interior, as in Figure 8, nor in the edge regions, as in Figure 7.

It appears that in the small clouds that contain only small droplets, the water-vapour fluctuations are the dominant cause of the Bragg scatter. However, as the liquid-water content increases and the droplets grow larger, another contribution can come into play, namely the liquid-water fluctuations. By the time precipitation

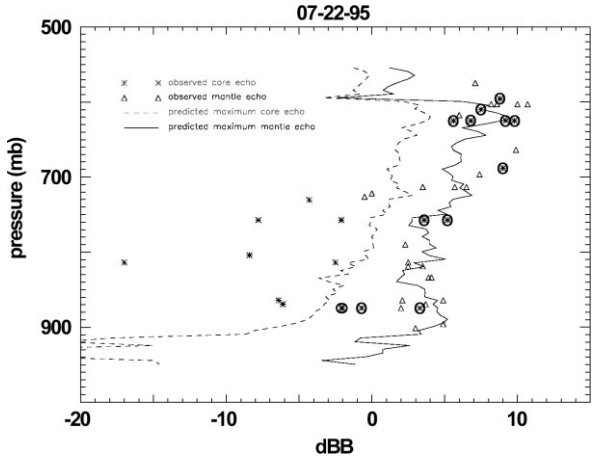

Figure 9. Predicted Bragg scatter, assuming that the water-vapour contribution is dominant, and the radar-observed values, plotted against pressure (height) on 22 July 1995. Lines and symbols are as in Figure 7. The cloud-interior points that exceed the prediction are circled for emphasis. Notice that the sounding-based predictions imply an increase in intensity with height. The edge observations fit this prediction quite well, whereas the observed core echo intensity increases with height more than predicted.

begins to form, the liquid-water contribution to the Bragg scatter has reached a value of about 5–10 dBB. Whether this contribution is significant depends on the magnitude of the water-vapour contribution which differs from day to day depending on the environmental sounding. On 6 August 1995, the water-vapour fluctuations were strong, and dominated the Bragg scatter. On 10 August, the water-vapour fluctuations were weak, and the liquid-water fluctuations came to dominate the Bragg scatter. On 22 July, the liquid-water fluctuations came to dominate for the cloud interiors but not for the cloud edges. As precipitation develops further, Rayleigh scatter dominates both radar, and no further observations of Bragg scatter in the cloud cores are possible.

7.2. Discussion of anomalous liquid-water fluctuations

Liquid-water fluctuations, as defined here, exceed those due merely to the random placement of the droplets: they refer to fluctuations in the *expected* value of the liquid-water content. This may be defined as the ensemble-averaged value in a volume around a given position, in the limit as the volume shrinks to zero. Consider the simple situation where all the droplets in a cloudy volume are randomly placed with equal probability at every position. At any given instant, the actual amount of liquid water in a finite volume would vary with location and time; however, the expected value of the liquid-water content would be constant throughout the cloudy volume.

The expected liquid-water content in clouds can vary because of mixing. However, if the liquid water were simply mixed like a passive scalar, its power spectrum would have a $-11/3$ slope in the inertial subrange (Tennekes and Lumley, 1972), and the contribution to the Bragg scatter would be negligible. This last fact is demonstrated in Figure 1(b), which shows the contributions to

DOI: 10.1002/qj

the relative-electric-permittivity fluctuations from many sources, including liquid-water fluctuations, assuming a $-11/3$ power law. The radar observations of Bragg scatter from liquid water therefore imply the existence of liquid-water fluctuations that significantly exceed those that would be expected if the liquid water were mixed as a passive scalar.

Analyses of high-rate liquid-water measurements in stratocumulus (Davis *et al*., 1999; Gerber *et al*., 2001) and in SCMS cumulus (Gerber *et al*., 2001) also suggest the existence of anomalous liquid-water fluctuations. This is observed via the liquid-water power spectrum, which can exhibit a scale break (at 2 m for cumulus and 5 m for stratocumulus), with a flattening of the slope at smaller scales. Gerber *et al*.note that this was observed only for some cumulus-cloud passes, while for others the measured one-dimensional liquid-water power spectrum followed the $-5/3$ slope all the way down to 20 cm, the smallest resolved scale. According to our interpretation of the observations presented above, the anomalous liquid-water fluctuations increase with cloud height, and thus, simultaneously, as the droplets increase in size. It would be interesting to determine whether the same correlation exists for the liquid-water power-spectrum indications of anomalous fluctuations.

The physical explanation of the anomalous fluctuations is uncertain. However, the observations are consistent with the following scenario. The larger the droplets, the more their inertia causes them to deviate from the turbulent-fluid paths. This causes them to congregate as they are thrown out of regions of high vorticity. Such an effect has been observed and modelled (Crisanti *et al*., 1992; Fung and Perkins, 1989; Lazaro and Lasheras, 1989; Squires and Eaton, 1991; Shaw *et al*., 1998; Vaillancourt, 1998), but for situations notably different from ours (Grabowski and Vaillancourt, 1999).

Given this (possible, but speculative) scenario, the SCMS radar observations may be explained as follows. When the droplets are small, they follow approximately fluid paths. The liquid-water power spectrum, like the water-vapour power spectrum, follows a $-11/3$ power law. The water vapour then dominates the Bragg scatter, and the expected maximum near the cloud edges is observed. As the drops grow larger, they begin to congregate at centimetre scales, causing their contribution to the Bragg scatter to increase. Whether the liquid-water contribution remains small compared with the water-vapour contribution, or comes to dominate it, causing a Bragg maximum in the interior where droplets are largest, depends on the environmental conditions. Notably, the magnitude of the water-vapour contribution to Bragg scatter varies with the environmental conditions, while the droplet contribution to Bragg scatter varies with the droplet sizes, and hence with height.

8. Conclusions

Radar observations of Bragg scatter from small cumulus clouds have been interpreted in conjunction with *in situ* aircraft measurements. A method of estimating the various Bragg terms from *in situ* aircraft observations has been derived and validated.

During the early stage of cumulus clouds, before collision and coalescence, Bragg scatter is caused by water-vapour fluctuations. The agreement between the predictions based on aircraft measurements and the radar observations is consistent over a variety of situations. The agreement exists across cloud where the magnitude of Bragg scatter can vary by two orders of magnitude. It exits across different days where the magnitude varies by one order of magnitude and it exists using different instruments on different aircraft. Thus, we have confidence in the theory of Bragg scatter and in our interpretations of the observations during the early stage in which Bragg scatter is caused by water-vapour fluctuations.

These interpretations include identification of large adiabatic cores, as well as regions of entrainment and mixing, and an estimation that the Kolmogorov microscale is on the centimetre scale.

Interpretation of the radar signals when the cloud droplets have grown larger is less straightforward than for the small-droplet clouds. Another source of Bragg scatter, apparently due to liquid-water fluctuations, comes into play. The existence of these anomalous fluctuations may have implications for understanding and modelling cloud-physical processes such as collision and coalescence.

Acknowledgements

This work was supported by NSF grant ATM-9420333 and Meteo-France. We gratefully acknowledge all the participants in the SCMS field project, in particular Charlie Knight and Jay Miller whose expertise and experience were invaluable during the project. We also thank Sharon Sessions, Kris Haskins, and Ueyn Block, excellent undergraduate students, for their part in the data analysis.

A. Appendix: Derivation of the radar equation

Here the radar equation is derived, including both the Rayleigh and the Bragg components, using a single mathematical model. At distances r much greater than the dimensions L of the radar, the magnitude of the outgoing electric field produced by linearly-polarized radar in a vacuum can be written as

$$E_{\mathrm{t}} = \frac{\sqrt{G(\theta,\phi)}}{r}\sqrt{\frac{P_{\mathrm{t}}}{2\pi c\varepsilon_0}}\cos(\omega t - kr), \qquad \text{(A1)}$$

where the radar is taken as the origin of a spherical coordinate system (r,θ,ϕ), P_{t} is the transmitted power, G is the normalized antenna gain, satisfying

$$\int_0^{\pi}\int_0^{2\pi} G(\theta,\phi)\sin\phi\,\mathrm{d}\theta\,\mathrm{d}\phi = 4\pi,$$

DOI: 10.1002/qj

c is the speed of light, ε_0 is the electric permittivity of free space, ω is the angular frequency of the radar, $k = 2\pi/\eta$ where η is the wavelength, and t is time. The direction of the electric field is perpendicular to $\mathbf{r}$.

Consider a single scatterer of size $\ll \eta$ at $r \gg L$. The dipole moment induced in the scatterer can be written as $4\pi\varepsilon_0\gamma E_\mathrm{t}$, where γ is the polarizability of the scatterer (In general, γ is a tensor relating the induced vector dipole moment $\mathbf{p}$ and the imposed vector electric field E_t, but here isotropic scattering is assumed: the direction of $\mathbf{p}$ and E_t are the same, and the ratio of their magnitudes is the scalar γ.). The magnitude of the electric field at the radar due to this oscillating dipole is

$$\gamma k^2 \frac{\sqrt{G(\theta,\phi)}}{r^2}\sqrt{\frac{P_\mathrm{t}}{2\pi c\varepsilon_0}}\cos(\omega t - 2kr). \tag{A2}$$

For multiple scatterers, the resultant electric field is the sum of the individual electric fields. Standard textbooks on electricity and magnetism provide derivations of the above expressions, which are good approximations in the atmospheric situation under consideration. It is also a valid approximation to ignore multiple scatter. Because the radar is pulsed, the sum is over a finite volume of depth $c\tau/2$, where τ is the duration of the pulse. Thus the magnitude of the relevant component of returning electric field at the radar is

$$E_\mathrm{r} = k^2\sqrt{\frac{P_\mathrm{t}}{2\pi c\varepsilon_0}}\int_{R-\frac{c\tau}{4}}^{R+\frac{c\tau}{4}}\int_0^\pi\int_0^{2\pi}\sqrt{G(\theta,\phi)} \times r^{-2}\cos(\omega t - 2kr)\sum_i \gamma_i\,\mathrm{d}N_i, \tag{A3}$$

where $R = c\Delta t/2$, Δt is the time between emission of the pulse (measured from the centre of the pulse) and measurement of the power, and $\mathrm{d}N_i$ is a stochastic differential that represents the number of type-i scatterers in the volume

$$\mathrm{d}V = r^2\sin\phi\,\mathrm{d}\theta\,\mathrm{d}\phi\,\mathrm{d}r.$$

The sum over i, and subscripts i on γ and on $\mathrm{d}N$, are included for the case where there is more than one type of scatterer. The differential $\mathrm{d}N_i$ can be thought of as $N_i\,\mathrm{d}V$ where N_i is a sum of delta functions at the locations of the type-i scatterers. The expected value of $\sum_i \gamma_i N_i$ is the deviation of the relative permittivity or dielectric constant ($\varepsilon/\varepsilon_0$, where ε is the electric permittivity) from 1.

The instantaneous values of E_r vary considerably because of movement of the scatterers. The radar measures the power received, P_r (which is proportional E_r^2), averaged over some time period that is sufficiently short so that the resolution in the range remains around $c\tau/2$. This does not sufficiently suppress the fluctuations, so a number M of returns from nearly the same volume are averaged. Thus, Equation (3) must be squared and averaged. It must also be multiplied by the constant of proportionality C_1 between E_r^2 and P_r. For the purposes of derivation, the average is considered to be an ideal ensemble average, and is denoted by an overbar. The actual radar measure is then an estimate of this ensemble average. Assuming statistical homogeneity of the M samples, the estimate improves with increasing M. Thus:

$$P_\mathrm{r} = C_1k^4\frac{P_\mathrm{t}}{2\pi c\varepsilon_0}\int_V\int_V\sqrt{G(\theta_1,\phi_1)}\sqrt{G(\theta_2,\phi_2)} \times r_1^{-2}r_2^{-2}\cos(\omega t - 2kr_1)\cos(\omega t - 2kr_2) \times \sum_i\sum_j \gamma_i\gamma_j\,\overline{\mathrm{d}N_i(\mathbf{r}_1)\,\mathrm{d}N_j(\mathbf{r}_2)}, \tag{A4}$$

where

$$\int_V \equiv \int_{R-\frac{c\tau}{4}}^{R+\frac{c\tau}{4}}\int_0^\pi\int_0^{2\pi}$$

and ideally $G(\theta,\phi)$ is zero except in a small range, typically of the order of 1°, in both θ and ϕ. The expected number of type-i scatterers in the volume $\mathrm{d}V$ is

$$\overline{\mathrm{d}N_i(\mathbf{r})} = \lambda_i(\mathbf{r})\,\mathrm{d}V.$$

Here $\lambda_i(\mathbf{r})$ is the number concentration of the type-i scatterers at the position $\mathbf{r}$. If $i \neq j$ or $\mathbf{r}_1 \neq \mathbf{r}_2$, then each realization, in the ensemble, of $\mathrm{d}N_i(\mathbf{r}_1)$ is independent of the corresponding realization of $\mathrm{d}N_j(\mathbf{r}_2)$, so

$$\overline{\mathrm{d}N_i(\mathbf{r}_1)\,\mathrm{d}N_j(\mathbf{r}_2)} = \left(\overline{\mathrm{d}N_i(\mathbf{r}_1)^2} - \left(\lambda_i(\mathbf{r}_1)\,\mathrm{d}V_1\right)^2\right)\delta_{ij}\delta(\mathbf{r}_1 - \mathbf{r}_2) + \lambda_i(\mathbf{r}_1)\lambda_j(\mathbf{r}_2)\,\mathrm{d}V_1\,\mathrm{d}V_2, \tag{A5}$$

where δ_{ij} is Kronecker's delta and $\delta(\mathbf{r}_1 - \mathbf{r}_2)$ is Dirac's delta function. To evaluate $\overline{\mathrm{d}N_i(\mathbf{r})^2}$, we assume that the positioning of the scatterers is a general Poisson process: they are randomly positioned, but the number concentration λ_i may vary spatially. Since, for a Poisson process, the variance equals the mean, i.e.

$$\overline{\mathrm{d}N_i(\mathbf{r})^2} - \left(\lambda_i(\mathbf{r})\,\mathrm{d}V\right)^2 = \lambda_i(\mathbf{r})\,\mathrm{d}V,$$

Equation (4) becomes:

$$P_\mathrm{r} = C_1k^4\frac{P_\mathrm{t}}{2\pi c\varepsilon_0} \times \left(\int_V G(\theta,\phi)r^{-4}\cos^2(\omega t - 2kr)\sum_i \gamma_i^2\lambda_i(\mathbf{r})\,\mathrm{d}V + \int_V\int_V\sqrt{G(\theta_1,\phi_1)}\sqrt{G(\theta_2,\phi_2)} \times r_1^{-2}r_2^{-2}\cos(\omega t - 2kr_1)\cos(\omega t - 2kr_2) \times \sum_i\sum_j \gamma_i\gamma_j\lambda_i(\mathbf{r}_1)\lambda_j(\mathbf{r}_2)\,\mathrm{d}V_1\,\mathrm{d}V_2\right) \tag{A6}$$

DOI: 10.1002/qj

The first term represents Rayleigh scattering, and is proportional to a weighted integral over the radar volume of the local quantity

$$\sum_i \gamma_i^2 \lambda_i(\mathbf{r}).$$

When $c\tau \ll R$ and $\sum_i \gamma_i^2 \lambda_i$ is uniform over the volume, variations in the weighting function

$$G^2(\theta, \phi) r^{-4} \cos^2(\omega t - 2kr)$$

are not important.

The second term, which can be written as

$$C_1 k^4 \frac{P_\mathrm{t}}{2\pi c \varepsilon_0} \left(\int_V \sqrt{G(\theta, \phi)} r^{-2} \times \cos(\omega t - 2kr) \sum_i \gamma_i \lambda_i(\mathbf{r}) \, \mathrm{d}V \right)^2,$$

is commonly referred to as Bragg scatter. If we take

$$G(\theta, \phi) r^{-2}$$

as constant in the radar volume and zero elsewhere, then this term may be interpreted physically. It is proportional to the square of the coefficient of the $2k$ term of the Fourier series for

$$\int_{\theta_\mathrm{min}}^{\theta_\mathrm{max}} \int_{\phi_\mathrm{min}}^{\phi_\mathrm{max}} \sum_i \gamma_i \lambda_i(\mathbf{r}) r^2 \sin\phi \, \mathrm{d}\phi \, \mathrm{d}\theta :$$

that is, the power at wave number $2k$ in the Fourier series of the above function of $(\mathbf{r})$. Since the beam is narrow, this is essentially the same as the $2\mathbf{k}$ term of the Fourier series of the three-dimensional correlation function of $\sum_i \gamma_i \lambda_i(\mathbf{r})$, where $|\mathbf{k}| = k$ and the direction of $\mathbf{k}$ is the direction of the radar beam.

In more physical language, the Rayleigh term depends on the concentration and size of the scatterers, while the Bragg term depends on spatial fluctuations of the relative electric permittivity,

$$1 + \sum_i \gamma_i \lambda_i(\mathbf{r}).$$

B. Appendix: Estimating the radar signal from *in situ* aircraft measurements

The functions $\lambda_i(\mathbf{r})$ in Equation (6) are not directly measurable. However, variables such as temperature, water-vapour mixing ratio, and liquid-water content are measured (Liquid-water content was measured with CSIRO hot-wire probes (King *et al.*, 1978), water-vapour mixing ratio with Lyman alpha hygrometers, and temperature with Rosemount probes.). In the following, we rewrite Equation (6) in terms of those measurable variables, so that we may compare radar observations with *in situ* aircraft observations.

It is possible to account for each type of molecule explicitly, but this is not necessary if they are well-mixed or rare. Trace constituents are ignored, and, since air is generally very well mixed except for water vapour, only two types of molecule are considered: dry air molecules and water-vapour molecules. In situations where CO_2 is not well mixed, it should be explicitly handled, as water vapour is here. Insects and aerosol are also ignored in this derivation. Scattering from insects can be significant in the boundary layer (Wilson *et al.*, 1994). Knight and Miller (1998) discuss insects as sources of radar backscatter in Florida, concluding that, while they probably do contribute to radar signals in the SCMS data in some circumstances, they are not responsible for the main features of concern to us here. The only other scatterers are water droplets of various sizes, which are assumed to be spherical and small in relation to the radar wavelength.

Assuming, as discussed in Appendix A, that

$$G(\theta, \phi) r^{-2}$$

and

$$G(\theta, \phi) r^{-4} \cos^2(\omega t - 2kr)$$

can be replaced with their average values in the radar volume, and letting

$$C_2 = C_1 k^4 G P_\mathrm{t} (2\pi c \varepsilon_0)^{-1} r^{-4},$$

the Rayleigh term can be succinctly written as

$$\frac{1}{2} V C_2 \sum_i \gamma_i^2 \Lambda_i \tag{A7}$$

where

$$\Lambda_i = \frac{1}{V} \int_V \lambda_i(\mathbf{r}) \, \mathrm{d}V$$

is the average number concentration of type-i scatterers in the radar volume. Note that we are now using the notation

$$\int_V \equiv \int_{R-\frac{c\tau}{2}}^{R+\frac{c\tau}{2}} \int_{\phi_\mathrm{min}}^{\phi_\mathrm{max}} \int_{\theta_\mathrm{min}}^{\theta_\mathrm{max}}.$$

Since γ^2 is small for molecules, the only significant Rayleigh contribution is from droplets, when they are present. For droplets,

$$\gamma_i^2 = \left| \frac{\varepsilon_\mathrm{b} - 1}{\varepsilon_\mathrm{b} + 2} \right|^2 d_i^6,$$

where d_i are the droplet diameters and ε_b is the complex dielectric constant of bulk water (Jackson, 1975, p. 149). Thus the Rayleigh term can be written as

$$\frac{1}{2} \left| \frac{\varepsilon_\mathrm{b} - 1}{\varepsilon_\mathrm{b} + 2} \right|^2 V C_2 \sum_i \Lambda_i d_i^6 = \frac{1}{2} \left| \frac{\varepsilon_\mathrm{b} - 1}{\varepsilon_\mathrm{b} + 2} \right|^2 V C_2 Z, \tag{A8}$$

DOI: 10.1002/qj

where by definition

$$Z = \sum \Lambda_i d_i^6.$$

Typically, radar processing returns

$$10 \log_{10} \frac{2P_r}{|\frac{\varepsilon_b - 1}{\varepsilon_b + 2}|^2 V C_2},$$

which, if the Rayleigh term dominates the signal, is

$$10 \log_{10} Z,$$

but more generally can be considered as

$$10 \log_{10} Z_e,$$

where Z_e is an effective Z.

The total Bragg term is

$$C_2 \left(\int_V \cos(\omega t - 2kr) \sum_i \gamma_i \lambda_i(\mathbf{r}) \, dV \right)^2, \tag{A9}$$

where

$$\sum_i \gamma_i \lambda_i(\mathbf{r}) = \gamma_{dry} \lambda_{dry}(\mathbf{r}) + \gamma_{vap} \lambda_{vap}(\mathbf{r}) + \sum_i \gamma_{d_i} \lambda_{d_i}(\mathbf{r}). \tag{A10}$$

Here the subscript 'dry' indicates dry air, subscript 'vap' indicates water vapour, and subscript d_i indicates a droplet of diameter d_i. We first consider the sum of the droplet terms:

$$\sum_i \gamma_{d_i} \lambda_{d_i}(\mathbf{r}) = \left| \frac{\varepsilon_b - 1}{\varepsilon_b + 2} \right| \sum_i \lambda_{d_i}(\mathbf{r}) d_i^3 = \left| \frac{\varepsilon_b - 1}{\varepsilon_b + 2} \right| \frac{6}{\pi \rho_l} \overline{LWC(\mathbf{r})},$$

where LWC is the liquid water content (in gm^{-3}) and $\rho_l = 10^6 \ \mathrm{gm}^{-3}$ is the density of liquid water. The overbar on LWC emphasizes the fact that because the λ_i are expected values, so is the LWC in this term. At any given instant, the liquid water is in the discrete droplets, and it makes no sense to talk about $LWC(\mathbf{r})$ unless it is a well-defined function: for example, the liquid water in a finite volume centred on $\mathbf{r}$; or the expected value as that volume shrinks to zero. The former definition has fluctuations due to random placement; the latter does not. This applies to any physical measurement. We mention it here because this distinction between fluctuations due to random placements and fluctuations in the expected value is analogous to the separation of radar return into distinct Rayleigh and Bragg terms. The Bragg term is due to fluctuations in the expected value of electric permittivity, while the Rayleigh term is due to random placement of the scatterers. *In situ* measurements of LWC can also be separated into the two effects; this may be regarded as estimating $\overline{LWC(\mathbf{r})}$ by removing the additional variations due to sampling statistics (Pawlowska and Brenguier, 1997).

The remaining terms

$$\gamma_{dry} \lambda_{dry}(\mathbf{r}) + \gamma_{vap} \lambda_{vap}(\mathbf{r}) \tag{A11}$$

may be rewritten, using the ideal-gas law to relate number concentrations λ_i to temperature T and pressure P, as

$$\frac{P}{BT} \gamma_{dry} + \rho_v R_v \left(\frac{\gamma_v}{B} - \frac{\gamma_{dry}}{B} \right), \tag{A12}$$

where ρ_v is the density of water vapour, R_v is the gas constant for water vapour, and B is Boltzmann's constant.

At radar wavelengths, the temperature dependencies of

$$\left| \frac{\varepsilon_b - 1}{\varepsilon_b + 2} \right|$$

and γ_{dry} are weak, and these are regarded as constants:

$$\left| \frac{\varepsilon_b - 1}{\varepsilon_b + 2} \right| = 0.96$$

and

$$\frac{\gamma_{dry}}{B} = 1.55 \times 10^{-4} \ \mathrm{K \ mb^{-1}}.$$

Since the water molecule has a permanent electric dipole moment, γ_{vap}/B is better modelled as

$$C_3 + \frac{C_4}{T},$$

where

$$C_3 = 1.43 \times 10^{-4} \ \mathrm{K \ mb^{-1}}$$

and

$$C_4 = 7.4 \times 10^{-1} \ \mathrm{K^2 \ mb^{-1}}$$

(Doviak and Zrnic, 1992, p. 16). Our concern is with the variation of the entire quantity

$$\frac{P}{T} \frac{\gamma_{dry}}{B} + \rho_v R_v \left(C_3 - \frac{\gamma_{dry}}{B} \right) + \rho_v R_v \frac{C_4}{T} \tag{A13}$$

as P, ρ_v and T vary. This is estimated to first-order variations in T and ρ_v. The middle term is much smaller than the other terms, and so is ignored. Variations in P are also ignored, because their effect is small compared with the effects of variations in T and ρ_v. The variation may then be written as

$$-\left(\frac{P}{T_{ave}^2} \frac{\gamma_{dry}}{B} + \frac{\rho_{v\,ave} R_v C_4}{T^2} \right) \delta T + \frac{R_v C_4}{T_{ave}} \delta \rho_v, \tag{A14}$$

where

$$\delta T(\mathbf{r}) = T(\mathbf{r}) - T_{ave} \ll T_{ave}$$

and

$$\delta \rho_v(\mathbf{r}) = \rho_v(\mathbf{r}) - \rho_{v\,ave}.$$

DOI: 10.1002/qj

(Note that these averages are spatial averages of quantities that are already ensemble-averaged.) This must be added to

$$\left|\frac{\varepsilon_b - 1}{\varepsilon_b + 2}\right| \frac{6}{\pi \rho_l} \delta\overline{LWC(\mathbf{r})},$$

where

$$\delta\overline{LWC(\mathbf{r})} = \overline{LWC(\mathbf{r})} - \overline{LWC(\mathbf{r})}_{\text{ave}},$$

and plugged back into Equation (9). This gives us

$$C_2 \left(\int_V \cos(\omega t - 2kr) \times \left(C_5 \delta\overline{LWC(\mathbf{r})} - C_6 \delta T + C_7 \delta\rho_v \right) \mathrm{d}V \right)^2 \quad \text{(A15)}$$

for the Bragg-scatter contribution to P_r, where C_5, C_6 and C_7 are given below together with the other constants C_n.

Since $\overline{LWC}$, T and ρ_v are not measured with high-enough spatial resolution to allow us to estimate the above integral directly, the square is expanded and each of the resulting terms is estimated from data and theory. Including the droplet Rayleigh term, there are seven potentially-significant contributions to P_r. These are given as (16) to (22) below. In these expressions, C_1 is the constant of proportionality between E_r^2 and P_r,

$$\begin{aligned}
C_2 &= C_1 k^4 G P_t (2\pi c \varepsilon_0)^{-1} r^{-4}, \\
C_3 &= 1.43 \times 10^{-4}\ \text{K mb}^{-1}, \\
C_4 &= 7.4 \times 10^{-1}\ \text{K}^2\ \text{mb}^{-1}, \\
C_5 &= \left|\frac{\varepsilon_b - 1}{\varepsilon_b + 2}\right| \frac{6}{\pi \rho_l} = 1.76 \times 10^{-6}, \\
C_6 &= P T_{\text{ave}}^{-2} \gamma_{\text{dry}} B^{-1} + \rho_{v\,\text{ave}} R_v C_4 T_{\text{ave}}^{-2} \\
&= 1.55 \times 10^{-4}\ \text{K mb}^{-1} \cdot P T_{\text{ave}}^{-2} \\
&\quad + 3.4 \times 10^{-3}\ \text{m}^3\text{g}^{-1}\ \text{K} \cdot \rho_{v\,\text{ave}} T_{\text{ave}}^{-2},
\end{aligned}$$

and

$$C_7 = R_v C_4 T_{\text{ave}}^{-1} = 3.4 \times 10^{-3}\ \text{m}^3\text{g}^{-1}\text{K} \cdot T_{\text{ave}}^{-1}.$$

The contributions are:

$$\sum_i \Lambda_i d_i^6 = Z, \quad \text{(A16)}$$

$$\left|\frac{\varepsilon_b - 1}{\varepsilon_b + 2}\right|^{-2} C_5^2 \frac{2}{V} \left(\int_V \cos(\omega t - 2kr) \times \delta\overline{LWC(\mathbf{r})}\, \mathrm{d}V \right)^2, \quad \text{(A17)}$$

$$\left|\frac{\varepsilon_b - 1}{\varepsilon_b + 2}\right|^{-2} C_6^2 \frac{2}{V} \left(\int_V \cos(\omega t - 2kr) \delta T(\mathbf{r})\, \mathrm{d}V \right)^2, \quad \text{(A18)}$$

$$\left|\frac{\varepsilon_b - 1}{\varepsilon_b + 2}\right|^{-2} C_7^2 \frac{2}{V} \left(\int_V \cos(\omega t - 2kr) \delta\rho_v(\mathbf{r})\, \mathrm{d}V \right)^2, \quad \text{(A19)}$$

$$-2\left|\frac{\varepsilon_b - 1}{\varepsilon_b + 2}\right|^{-2} C_5 C_6 \frac{2}{V} \times \left(\int_V \cos(\omega t - 2kr) \delta\overline{LWC(\mathbf{r})}\, \mathrm{d}V \right) \times \left(\int_V \cos(\omega t - 2kr) \delta T(\mathbf{r})\, \mathrm{d}V \right), \quad \text{(A20)}$$

$$2\left|\frac{\varepsilon_b - 1}{\varepsilon_b + 2}\right|^{-2} C_5 C_7 \frac{2}{V} \times \left(\int_V \cos(\omega t - 2kr) \delta\overline{LWC(\mathbf{r})}\, \mathrm{d}V \right) \times \left(\int_V \cos(\omega t - 2kr) \delta\rho_v(\mathbf{r})\, \mathrm{d}V \right), \quad \text{(A21)}$$

and

$$-2\left|\frac{\varepsilon_b - 1}{\varepsilon_b + 2}\right|^{-2} C_5 C_7 \frac{2}{V} \times \left(\int_V \cos(\omega t - 2kr) \delta T(\mathbf{r})\, \mathrm{d}V \right) \times \left(\int_V \cos(\omega t - 2kr) \delta\rho_v(\mathbf{r})\, \mathrm{d}V \right). \quad \text{(A22)}$$

Each of the terms (16) to (22) has been divided by

$$\frac{1}{2}\left|\frac{\varepsilon_b - 1}{\varepsilon_b + 2}\right|^2 C_2 V,$$

because radar typically display

$$10 \log_{10}\left(\frac{2P_r}{C_2 V} \left|\frac{\varepsilon_b - 1}{\varepsilon_b + 2}\right|^{-2} \right)$$

and label this dBZ, assuming that the term (16) dominates over the other terms. However, we are interested in cases where the term (16) is not necessarily dominant. Thus, we call

$$10 \log_{10} \sum_i \Lambda_i d_i^6$$

dBZ, and we call

$$10 \log_{10}\left(\frac{2P_r}{C_2 V} \left|\frac{\varepsilon_b - 1}{\varepsilon_b + 2}\right|^{-2} \right)$$

for the 10 cm and 3 cm radar respectively dBZ_{eS} and dBZ_{eX}, to emphasize that they are *effective* reflectivities. For the Bragg signal, we consider what dBZ_{eS} would be if Z were zero (using the common radar units of $\text{mm}^6\ \text{m}^{-3}$), and call this dBB.

The term (16) is easy to calculate from aircraft measurements of the droplet sizes and concentrations.

DOI: 10.1002/qj

The terms (17), (18) and (19) are all of the form

$$\frac{2}{V}\left(\int_V \cos(\omega t - 2kr) f(\mathbf{r})\,\mathrm{d}V\right)^2.$$

Each of the functions $f(\mathbf{r})$ is a physical variable measured *in situ* via the aircraft. However, these are three-dimensional integrals, while the measurements are essentially one-dimensional. Furthermore, the spatial resolution of the measurements is much too coarse for these integrals to be computed directly. Therefore, we need some assumptions in order to estimate them. The functions $f(\mathbf{r})$ are assumed to be homogeneous, isotropic random functions. This gives a theoretical relation between the three-dimensional quantities and the one-dimensional measurements. We also assume that the power spectrum of the measurements follows a $-5/3$ power law on scales from 100 m to half the radar wavelength (5 cm). This allows extrapolation to the desired small scales from the larger measurable scales.

On pages 99–102 of Lumley's book *Stochastic Tools in Turbulence*, the following relation for isotropic homogeneous random functions on the infinite domain is derived:

$$\left|\int_{-\infty}^{\infty}\int_{-\infty}^{\infty}\int_{-\infty}^{\infty} \mathrm{e}^{\mathrm{i}\mathbf{k}\cdot\mathbf{x}} f(\mathbf{x})\,\mathrm{d}\mathbf{x}\right|^2 = F_3(k') = -\frac{2\pi}{k'}\frac{\partial F_1(k')}{\partial k'}, \tag{A23}$$

where

$$F_1(k') = \left|\int_{-\infty}^{\infty} \mathrm{e}^{\mathrm{i}k'x} f(x)\,\mathrm{d}x\right|^2. \tag{A24}$$

Our other assumption is that

$$F_1(k') = C_n k'^{-\frac{5}{3}},$$

so that

$$F_3(k') = \frac{10\pi}{3} C_n k'^{-\frac{11}{3}}. \tag{A25}$$

As an estimate, we use

$$F_1(k') \approx \frac{1}{L}\left|\int_{-L/2}^{L/2} \mathrm{e}^{\mathrm{i}k'x} f(x)\,\mathrm{d}x\right|^2, \tag{A26}$$

and we use Riemann sums to estimate this finite-domain integral from the discrete aircraft measurements of $f(x)$. We then estimate C_n by dividing our $F_1(k')$ estimate by $k'^{-5/3}$ and taking the mean. Finally, we estimate

$$\frac{2}{V}\left(\int_V \cos(\omega t - 2kr) f(\mathbf{r})\,\mathrm{d}V\right)^2$$

as $F_3(2k)$.

The terms (20), (21) and (22) are the cross terms in the expansion of the square in Equation (15). These are the most difficult of the terms to estimate. They can be either positive or negative. However, if one of (17), (18) or (19) dominates the other two, then it also dominates the cross terms. Therefore, these cross terms will not be of great significance unless two of the terms (17), (18) and (19) are close in magnitude and the functions are well correlated. Generally, the water-vapour term (19) dominates the Bragg-scatter contribution, and so we do not need to consider the cross terms any further here. In Section 7, we discuss the likelihood that the liquid-water term exceeds the water-vapour term. When they are comparable, we cannot in principle ignore the cross term, but as we expect the water vapour and liquid water to be mostly uncorrelated, we do not attempt to estimate the cross term.

References

Blyth AM, Latham J. 1997. A multi-thermal model of cumulus glaciation via the Hallett-Mossop process. *Q. J. R. Meteorol. Soc.* **123**: 1185–1198.

Blyth AM, Lasher-Trapp SG, Cooper WA. 2005. A study of thermals in cumulus clouds. *Q. J. R. Meteorol. Soc.* **131**: 1171–1190.

Chapman DR. 1979. Computational aerodynamics development and outlook. *AIAA*. **17**: 1293–1313.

Crisanti A, Falcioni M, Provenzale A, Tanga P, Vulpiani A. 1992. Dynamics of passively advected impurities in simple two-dimensional flow models. *Physics of Fluids A: Fluid Dynamics*, **4**(8): 1805–1820.

Davis AB, Marshak A, Gerber H, Wiscombe WJ. 1999. Horizontal structure of marine boundary-layer clouds from cm to km scales. *J. Geophys. Res.* **104**: 6123–6144.

Doviak RJ, Zrnic DS. 1992. *Doppler Radar and Weather Observations*. Academic Press.

Erkelens JS, Venema VKC, Russchenberg HWJ. 2001. Coherent scattering of microwaves by particles: Evidence from clouds and smoke. *J. Atmos. Sci.* **58**: 1091–1102.

Fung JCH, Perkins RJ. 1989. 'Particle trajectories in turbulent flow generated by true-varying random Fourier modes'. Pp 322–328 in: *Advances in Turbulence*, 2nd edition, Fernholz H, Fiedler H (eds). Springer, New York.

Gerber H, Jensen JB, Davis AB, Marshak A, Wiscombe WJ. 2001. Spectral density of cloud liquid water content at high frequencies. *J. Atmos. Sci.* **58**: 497–503.

Gossard EE, Strauch RG. 1983. *Radar Observation of Clear Air and Clouds*. Elsevier.

Gossard EE, Chadwick RB, Detman TR, Gaynor J. 1984. Capability of surface-based clear-air doppler radar for monitoring meteorological structure of elevated layers. *J. Clim. Appl. Meteorol.* **23**: 474–485.

Grabowski WW, Vaillancourt P. 1999. Comments on 'Preferential concentration of cloud droplets by turbulence: effects on the early evolution of cumulus cloud droplet spectra'. *J. Atmos. Sci.* **56**: 1433–1436.

Hill RJ. 1978. Spectra of fluctuations in refractivity, temperature, humidity, and the temperature–humidity cospectrum in the inertial and dissipation ranges. *Radio Sci.* **13**: 953–961.

Jackson JD. 1975. *Classical Electrodynamics*. Wiley: New York.

Jensen JB, Austin PH, Baker MB, Blyth AM. 1985. Turbulent mixing, spectral evolution and dynamics in a warm cumulus cloud. *J. Atmos. Sci.* **42**: 173–192.

King WD, Parkin DA, Handsworth RJ. 1978. A hot-wire liquid water device having fully calculable response characteristics. *J. Appl. Meteorol.* **17**: 1809–1813.

Knight CA, Miller LJ. 1998. Early radar echoes from small, warm cumulus: Bragg and hydrometeor scattering. *J. Atmos. Sci.* **55**: 2974–2992.

Lawson RP, Blyth AM. 1998. A comparison of optical measurements of liquid water content and drop size distribution in adiabatic regions of Florida cumuli. *Atmos. Res.* **47–48**: 671–690.

Lazaro BJ, Lasheras JC. 1989. Particle dispersion in a turbulent, plane, free shear layer. *Phys. Fluids* **1**: 1035–1044.

Lumley JL. 1970. *Stochastic Tools in Turbulence*. Academic Press, New York: 194 pp. ISBN: 124600506.

Mason BJ, Jonas PR. 1974. The evolution of droplet spectra and large droplets by condensation in cumulus clouds. *Q. J. R. Meteorol. Soc.* **100**: 23–38.

Pawlowska H, Brenguier JL. 1997. Optimal nonlinear estimation for cloud particle measurements. *J. Atmos. Oceanic Technol.* **14**: 88–104.

Shaw RA, Reade WC, Collins LR, Verlinde J. 1998. Preferential concentration of cloud droplets by turbulence: effects on the early evolution of cumulus cloud droplet spectra. *J. Atmos. Sci.* **55**: 1965–1976.

Squires KD, Eaton JK. 1991. Preferential concentration of particles by turbulence. *Phys. Fluids* **3**: 1169–1178.

Tennekes H, Lumley JL. 1972. *A First Course in Turbulence*. MIT Press: Cambridge, MA.

Vaillancourt P. 1998. *Microscopic Approach to Cloud Droplet Growth by Condensation*. PhD thesis, McGill University, Montreal.

Wilson JW, Weckwerth TM, Vivekanandan J, Wakimoto RM, Russell RW. 1994. Boundary layer clear-air radar echoes: Origin of echoes and accuracy of derived winds. *J. Atmos. Oceanic Technol.* **11**: 1184–1206.

DOI: 10.1002/qj